Phase-field model of oxidation: Equilibrium

Q. C. Sherman and P. W. Voorhees
Department of Materials Science and Engineering, Northwestern University, Evanston, Illinois 60208, USA
(Received 2 December 2016; published 2 March 2017)

A phase-field model of an oxide relevant to corrosion resistant alloys for film thicknesses below the Debye length L_D, where charge neutrality in the oxide does not occur, is formulated. The phase-field model is validated in the Wagner limit using a sharp interface Gouy-Chapman model for the electrostatic double layer. The phase-field simulations show that equilibrium oxide films below the Wagner limit are charged throughout due to their inability to electrostatically screen charge over the length of the film, L. The character of the defect and charge distribution profiles in the oxide vary depending on whether reduced oxygen adatoms are present on the gas-oxide interface. The Fermi level in the oxide increases for thinner films, approaching the Fermi level of the metal in the limit $L/L_D \to 0$, which increases the driving force for adsorbed oxygen reduction at the gas-oxide interface.

DOI: 10.1103/PhysRevE.95.032801

I. INTRODUCTION

Corrosion resistant alloys withstand complete oxidation by either preferentially forming or being coated by an oxide that has slow growth kinetics which deter continued oxide growth [1,2]. These protective oxide phases have such low ionic conductivity that growth effectively stops after a continuous layer has formed. Two of the most common protective oxide phases are Cr_2O_3 and Al_2O_3, which provide corrosion resistance in many high temperature alloys [3]. Although these oxides are thermodynamically preferred to the oxide phases of the metals they are commonly alloyed with for high temperature applications; alloy concentration and kinetic effects often lead to the nucleation of multiple oxide phases during the onset of oxidation, which can have a strong effect on the resulting morphology and composition of the surface oxide layer at later stages [4–8].

Bridging the gap between thin and thick scale oxide growth models is a well-known challenge, where thin and thick are defined relative to the electronic screening length in the oxide [9–12]. The most widely accepted theories for these two limiting cases are the Cabrera-Mott [13] and Wagner [14] models, which have been reviewed by Atkinson [11]. Both models rely on a single process being rate limiting: cation injection in the Cabrera-Mott limit and diffusion in the Wagner limit. A more complete model must address a number of coupled physical processes in order to connect the two regimes, namely, interfacial redox reactions, mass and charge transport, and electrostatics. The coupling of these processes is crucial to describing oxide growth, but the ensuing mathematical complexities of the model require a numerical treatment [12,15].

Here we employ a phase-field method to model an electrochemical oxide-metal interface in contact with a gas. The phase-field method is a logical approach for modeling a system with multiple physical processes coupled at a moving interface [16]. The method replaces a sharp interface description of a two-phase boundary with a diffuse one, allowing the governing equations to be continuous across a multiphase system. The phase-field variable generally takes on a distinct value in each phase and interpolates bulk properties smoothly through the interfacial region. We treat the interfacial region as a two phase mixture with distinct phase compositions, following the Kim-Kim-Suzuki (KKS) and Steinbach models [17,18]. The KKS model decouples the equilibrium interfacial energy and thickness from the chemical free energy expressions and is better suited for treating systems with steep free energy composition curves, as is the case for most metal oxides. Although not addressed here, it is relatively straightforward to add multiple crystallographic orientations and additional free energy contributions such as that stemming from strain to a phase-field model, which will be important in developing better models of oxide-metal interfaces in the future [19,20]. In the present study we focus on the addition of the electrostatic free energy contribution to the system to model the electrostatic double layer at the interface. Treating the electrostatic double layer is important for modeling scales between the Cabrera-Mott and Wagner regimes, but is computationally challenging due to the exponential decay of space charge away from interfaces, which requires an extremely fine numerical resolution to model accurately [10,21]. We employ the simplest defect structure that allows for oxide growth in order to avoid complications such as multiple moving interfaces and defect-defect interactions.

Phase-field models of electrochemical interfaces, first developed by Guyer *et al.* [22,23], have been used to model a few one-dimensional electrochemical systems [24,25]. Guyer *et al.* studied an electrolyte-electrode interface and showed that the charge distribution and electrostatics agree with classic electrochemical interface theory and that the differential capacitance curves diverge from theory but qualitatively agree with the complex curves seen in experiment [22]. A continuing difficulty with electrochemical phase-field models is understanding the interplay between the electrostatic double layer and structural interface, as a closed-form solution for the interfacial free energy and thickness are not currently known. Here we solve the governing equations for an equilibrium oxide film to demonstrate that for protective oxide phases such as Cr_2O_3 and Al_2O_3, the Debye length and structural interface width are disparate enough to treat them independently. This is validated with a sharp interface description of the electrostatic double layer.

II. MODEL BACKGROUND

Two structural interfaces develop as an oxide layer forms on the surface of a metal: a gas-oxide and oxide-metal interface.

The oxide layer can grow or shrink by the migration of either interface, with the velocities of the two interfaces being determined by reaction thermodynamics, interface kinetics, and relative mobilities of the defect structures in the oxide. Anion and cation transport facilitate the motion of the oxide-metal and gas-oxide interfaces, respectively. In a standard phase-field model of a phase transformation, the length scale of each moving structural interface is defined by the equilibrium phase-field interfacial thickness, whereas in a sharp interface description this interface has zero thickness [16]. In the present study we will only consider anion diffusion in the oxide, so that only the oxide-metal interface is in motion. In this case we only need to treat the oxide-metal interface with a phase-field description because the gas-oxide interface is stationary.

In addition to the structural interfaces, charged double layers develop at phase boundaries in electrochemical systems. The double layers form due to the differences in equilibrium chemical potentials of the charged species in the materials [26]. An associated electrostatic potential difference, referred to as the Galvani potential, develops between the bulk phases that equilibrates the electrochemical potentials across the system. The space charge composing the double layer decays exponentially in the bulk phases due to screening by mobile charge carriers, with a characteristic length scale given by the material's screening length, referred to as the Debye length in semiconductors, classically defined as [27]

$$L_D = \sqrt{\frac{\varepsilon^O k_B T}{e^2 c_d}}, \tag{1}$$

where c_d is the native charged defect density (moles of elementary charge/m^3) in the oxide, ε^O is the permittivity of the oxide, and e is the elementary charge. Protective oxide phases have Debye lengths on the order of tens or hundreds of nanometers due to their low native defect concentrations [11].

Wagner derived the well-known parabolic growth law for diffusion limited oxide growth by assuming the oxide scale is large compared to its Debye length [14]. In other words, Wagner assumed that the length scale of the electrostatic double layer is very short compared to the oxide scale thickness, which means that the spatial variations in the electrostatics are localized at the interfaces. Under this assumption the space charge in the bulk oxide is zero, which results in a spatially invariant electric field from Gauss's law. Wagner then assumed a coupled currents condition in the oxide, or that the net current is zero everywhere. With these assumptions the interfacial charging is constant in time and the electric field can be incorporated into an effective diffusivity for ionic and electronic transport. Wagner's assumptions break down, however, when oxide thickness is not significantly greater than the Debye length. When the oxide thickness is on the order of the Debye length, the space charge can no longer be considered localized at the interfaces. In this case, the spatially resolved electric field must be treated in the bulk oxide to accurately model growth. Since, from Eq. (1), the Debye length in an oxide scales with its defect density as $L_D \propto c_d^{-1/2}$, modeling the growth of oxide scales below the Wagner limit is particularly important to understanding the growth kinetics of protective oxide scales, which tend to have low defect densities [11].

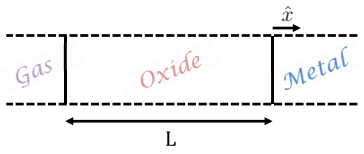

FIG. 1. Schematic of a uniform oxide scale of thickness L grown on a metal surface in gas.

III. MODEL DESCRIPTION

We consider a single oxide phase O (Metal Oxide) growing on a metal M after a thin continuous layer of thickness L and area $\mathcal{A}$ has nucleated on the surface, shown schematically in Fig. 1. The coordinate system is chosen such that $\hat{\boldsymbol{x}}$ is in the growth direction and the oxide film is uniform in the $\hat{\boldsymbol{y}}$ and $\hat{\boldsymbol{z}}$ directions. In order to avoid considering volume expansion during oxide formation, the lattice constants in the oxide and metal are treated as equal. The oxide defect structure consists of neutral anion vacancies, V_A, and electrons e^-, as is known to be reflective of alumina growth where oxygen vacancies are the primary diffusing species [28]. By only treating neutral anion vacancies we avoid having to consider defect-defect interactions in the oxide that would need to be accounted for if multiple ionic defects were included [29,30]. Although this is a simplification of the defect structure, it has been shown to capture the coupling of the spatially resolved electric field with ionic diffusion that we are interested in [28,31,32]. The electrons in the oxide are localized on the cation sublattice, so that they have the same configurational entropy contribution as the anion vacancies [33]. In this formulation, the conduction of negative charge in the oxide is dominated by electron hopping between cation sites as opposed to, for example, diffusion of negatively charged cations or a conduction band in the oxide [34].

With the preceding assumptions, the mole fractions X of electrons and anion vacancies in the oxide are given by

$$X_i = \frac{\text{molar density of } i}{\text{molar density of } i\text{'s sublattice}} \text{ for } i = e, v, \tag{2}$$

where e and v represent electrons and anion vacancies, and electrons reside on the cation sublattice. In order to avoid considering volume changes during diffusion, the molar volume of the anions and anion vacancies are assumed equal and the molar volume of the electrons is zero.

The metal is composed primarily of conduction electrons e^- and metal atoms M^+, with each metal atom contributing one electron to the conduction band. The electrons are treated as a free electron gas in the metal phase and the density of states at the Fermi level is assumed small enough so that the entropic contribution to the free energy of the electron gas is negligible [35]. We assume there are no defects in the metal phase, for example dissolved oxygen, that contribute significantly to the oxide growth. However, from a modeling perspective we cannot set the anion concentration in the metal equal to zero, and for this reason we must assume a small concentration of negatively charged oxygen defects in the metal. For simplicity, we treat these oxygen defects as interstitials so that they do not mix with the metal atoms on the metal lattice. A single interstitial site is associated with

each metal site so that the entropic free energy expression for the oxygen atoms is equivalent in both phases.

The molar densities of electrons e', anions $A_A^\times$, cations $M_M^\times$, and anion vacancies $V_A^\bullet$ (Kröger-Vink notation) in the oxide-metal system are denoted by c_e, c_a, c_m, and c_v, respectively, which have charge numbers $q_e = -1$, $q_a = q_m = 0$, and $q_v = 1$. For accounting purposes in the oxide, we also define electron holes $h^\times$ on the cation sublattice that represent cation sites that lack an extra electron. If we define C as the molar density of the sublattices in the oxide and metal, structure conservation requires

$$c_m = c_a + c_v = \mathrm{C} \quad \text{everywhere}, \tag{3}$$

$$c_e + c_h = \mathrm{C} \quad \text{in the oxide}, \tag{4}$$

which reflect that the cation molar density c_m is fixed and equal to C across the system, and that the sum of the anion and anion vacancy molar density must be equal to C everywhere. The sum of the electron and hole molar density must be equal to C in the oxide, but there is no structure conservation requirement for the free electron gas in the metal. Therefore the system can be fully described by the anion vacancy and electron densities. The molar densities are related to mole fractions defined by Eq. (2) as $X_i = c_i/\mathrm{C}$. Given the charge numbers of each species listed above, the defect density dependent charge density ρ is given by

$$\rho = \sum_{i=e,a,m,v} q_i c_i F = (c_v - c_e)F, \tag{5}$$

where F is Faraday's constant. The local electrostatic potential, ψ, in the system is related to the charge density through Gauss's law:

$$-\nabla \cdot [\varepsilon \boldsymbol{E}] = \nabla \cdot [\varepsilon \nabla \psi] = -\rho, \tag{6}$$

where ε is permittivity and $\boldsymbol{E}$ is the electric field. Although we do not impose local charge neutrality, the total charge in the system is conserved since there is no flux of charge into the oxide-metal system from the gas phase:

$$\int_V \rho \, dV = 0 \Rightarrow \int_V [c_v + c_e] dV = 0.$$

We only treat anion diffusion in the oxide; however it is straightforward to adjust the system to describe cation vacancy diffusion rather than anion vacancy diffusion, relevant to other oxides such as NiO [36]. In this case c_v would represent the cation vacancy density. In order to conserve charge in the oxide, mobile holes $h^\bullet$ would replace the conduction electrons e'. The corresponding defect charge numbers would be $q_h = 1$, $q_a = q_m = 0$, and $q_v = -1$. Structure conservation would require $c_a = c_m + c_v$ rather than $c_m = c_a + c_v$. The rest of the paper proceeds assuming anion vacancy diffusion.

A. Bulk phase thermodynamic formulation

According to Eqs. (3) and (4), an anion vacancy or electron cannot be created on their associated sublattices without removing an anion or hole. Therefore the chemical potential of these single species cannot be evaluated without violating structure conservation. To address this, we follow Lankhorst *et al.* by defining the following structure elements in the oxide:

$$\{V_A^\bullet\} = V_A^\bullet - A_A^\times \quad \text{and} \quad \{e'\} = e' - h^\times, \tag{7}$$

which represent an exchange of species occupying a particular sublattice site [30]. The structure elements have physical chemical potentials that can be evaluated as differences in the nonphysical chemical potentials of the individual species being exchanged.

We start by assuming an ideal solution model for the Gibbs free energy density of the oxide phase. The ideal solution model for the chemical part of the Gibbs free energy density of the oxide phase is

$$G^O_{\text{ideal}} = \mathrm{C}\left(\mu_m^{\circ O} + \mu_a^{\circ O}\right) + \sum_{i=v,e} c_i^O \left[\mu_{\{i\}}^{\circ O} + RT\left(\ln \frac{c_i^O}{\mathrm{C}} + \frac{\mathrm{C} - c_i^O}{c_i^O} \ln \frac{\mathrm{C} - c_i^O}{\mathrm{C}}\right)\right].$$

The quantity $\mu_m^{\circ O} + \mu_a^{\circ O}$ is the chemical potential of the defect-free oxide, which can be evaluated without violating structure conservation. The quantities $\mu_{\{i\}}^{\circ j}$ are the standard state chemical potentials of the structure elements defined in Eq. (7) and are differences in the single species standard state chemical potentials. For example, the standard state chemical potential of the vacancy structure element is given by $\mu_{\{v\}}^{\circ O} = \mu_v^{\circ O} - \mu_a^{\circ O}$.

The anion and electron contributions to the chemical Gibbs free energy density of the metal phase are treated with an ideal solution and free electron gas model, respectively. A structure element for the anions in the metal is defined in the same fashion as in Eq. (7) for the oxide phase. Since there is no condition of structure conservation for electrons in the metal, the chemical potential of a single electron in the metal is well defined. The chemical part of the Gibbs free energy density of the metal phase is

$$G^M_{\text{ideal}} = \mathrm{C}\mu_m^{\circ M} + \int_0^{c_e^M} \mu_e^M dc + \left(\mathrm{C} - c_v^M\right)\left[\mu_{\{a\}}^{\circ M} + RT\left(\frac{c_v^M}{\mathrm{C} - c_v^M} \ln \frac{c_v^M}{\mathrm{C}} + \ln \frac{\mathrm{C} - c_v^M}{\mathrm{C}}\right)\right].$$

As with the oxide, the quantity $\mu_m^{\circ M}$ is the chemical potential of the defect-free metal. The electron density dependent electron chemical potential μ_e^M is taken as the standard Fermi level expression from free electron gas theory [35]:

$$\mu_e^M = \frac{{N_A}^{5/3}\hbar^2(3\pi^2)^{2/3}}{2m_e}\left(c_e^M\right)^{2/3},$$

where $\hbar$ is the reduced Planck's constant, m_e is the mass of an electron, and N_A is Avogadro's number. To simplify the notation, we drop the brackets representing structure elements in the chemical potentials in the rest of the paper, but all defect chemical potentials still refer to structure element chemical potentials as defined in Eq. (7).

To make the problem more computationally tractable, we express the composition dependent chemical Gibbs free energy densities of the metal and oxide phases as second-order Taylor expansions about the two-phase equilibrium densities $c_{i,eq}^j$, for $i = e,v$ and $j = O,M$. We have taken advantage of the fact

that the bulk phases must be charge neutral at equilibrium, which from Eq. (5) implies that the equilibrium density of electrons and anion vacancies are equal in a given phase:

$$c_{eq}^{j} \equiv c_{e,eq}^{j} = c_{v,eq}^{j} \quad \text{for } j = O,M.$$

The Taylor expanded Gibbs free energy densities are given by

$$G^{j} = G^{\circ j} + \sum_{i=e,v}\left[\mu_{i,eq}^{j}\left(c_i^{j} - c_{eq}^{j}\right) + \frac{1}{2}B_i^{j}\left(c_i^{j} - c_{eq}^{j}\right)^2\right] \quad \text{for } j = O,M, \tag{8}$$

where $\mu_{i,eq}^{j} \equiv (\partial G_{\text{ideal}}^{j}/\partial c_i^{j})|_{c_{eq}^{j}}$ are the two-phase equilibrium chemical potentials, $B_i^{j} \equiv (\partial^2 G_{\text{ideal}}^{j}/\partial {c_i^{j}}^2)|_{c_{eq}^{j}}$ are the second derivatives of the free energy densities at equilibrium, and $G^{\circ j} \equiv G_{\text{ideal}}^{j}|_{c_{eq}^{j}}$ are the equilibrium free energy densities. The expressions for $\mu_{i,eq}^{j}$ and B_i^{j} are provided in Appendix A.

We can derive standard expressions for the chemical and electrochemical potentials of each species from the Gibbs free energy densities:

$$\mu_i^{j} = \frac{\partial G^{j}}{\partial c_i} = \mu_{i,eq}^{j} + B_i^{j}\left(c_i^{j} - c_{eq}^{j}\right),$$
$$\bar{\mu}_i^{j} = \mu_i^{j} + q_i F \psi^{j} \quad \text{for } i = e,v \quad \text{and} \quad j = O,M. \tag{9}$$

For convenience, we choose the arbitrary zero of the free energy scale to coincide with the equilibrium chemical free energy density of the oxide phase in two-phase equilibrium. The chemical Gibbs free energy densities can then be written

$$G^{O} = \sum_{i=e,v}\left[\mu_{i,eq}^{O}\left(c_i^{O} - c_{eq}^{O}\right) + \frac{1}{2}B_i^{O}\left(c_i^{O} - c_{eq}^{O}\right)^2\right], \tag{10}$$

$$G^{M} = \sum_{i=e,v}\left[\mu_{i,eq}^{M}\left(c_i^{M} - c_{eq}^{M}\right) + \frac{1}{2}B_i^{M}\left(c_i^{M} - c_{eq}^{M}\right)^2\right] + \Delta G^{\circ}, \tag{11}$$

where $\Delta G^{\circ} \equiv G^{\circ M} - G^{\circ O}$ is the difference in two-phase equilibrium Gibbs free energy densities, provided in Eq. (A4). The quantity ΔG° contains the difference between the chemical potentials of the defect-free metal and oxide structures $\Delta\mu^{\circ}$, defined by

$$\Delta\mu^{\circ} = \mu_m^{\circ M} - \mu_m^{\circ O} - \mu_a^{\circ O}. \tag{12}$$

B. Oxide-metal equilibrium

The oxide and metal phases are at equilibrium when there is zero driving force for phase transformation and the electrochemical potential of each species is uniform across the system. These conditions result in three equations for the two equilibrium defect densities and the equilibrium potential difference between the bulk phases, $\Delta\psi^{\circ} \equiv \psi_{eq}^{M} - \psi_{eq}^{O}$. The potential difference $\Delta\psi^{\circ}$ is the Galvani potential between the oxide and metal, a materials property related to the difference in equilibrium chemical potentials of charged species between the two materials [37,38]. The Galvani potential develops via the formation of the electrostatic double layer as charged species migrate to the material where they have a lower chemical potential. The Fermi level is typically lower in the oxide than in the metal, in which case ψ_{eq}^{M} will be higher than ψ_{eq}^{O}.

The driving force for phase transformation in the oxide-metal system, denoted by $\Pi_{o/m}$ with units of J/mol, can be derived from the chemical free energy densities in Eqs. (10) and (11) and the electrostatic free energy density:

$$\text{c}\Pi_{o/m} = G^{M}\left(c_v^{M}, c_e^{M}\right) - G^{O}\left(c_v^{O}, c_e^{O}\right) + \sum_{i=v,e}\left[\left(c_i^{O} - c_i^{M}\right)\mu_i^{O}\right] + \rho^{M}\psi^{M} - \rho^{O}\psi^{O}. \tag{13}$$

At equilibrium, the driving force must be zero:

$$\Pi_{o/m}|_{c_v^{O}=c_e^{O}=c_{eq}^{O},\, c_v^{M}=c_e^{M}=c_{eq}^{M}} = 0. \tag{14}$$

The equilibrium electrostatic potentials of the bulk phases ψ_{eq}^{O} and ψ_{eq}^{M} do not appear in Eq. (14) because the bulk phases are charge neutral at equilibrium. The condition of electrochemical equilibrium of each species is given by

$$\bar{\mu}_i^{M}|_{c_{eq}^{M},\psi_{eq}^{M}} = \bar{\mu}_i^{O}|_{c_{eq}^{O},\psi_{eq}^{O}} \quad \text{for } i = e,v. \tag{15}$$

Equations (14) and (15) uniquely determine the equilibrium densities and Galvani potential between the bulk phases. The Galvani potential is solved for by substituting Eq. (9) into Eq. (15) and rearranging to find $\psi^{M} - \psi^{O}$, and is given by

$$\Delta\psi^{\circ} = \frac{\mu_{i,eq}^{O} - \mu_{i,eq}^{M}}{q_i F} \quad \text{for } i = e,v. \tag{16}$$

C. Gas-oxide interface

The gas-oxide interface is treated as a sharp interface throughout the paper since zero cation diffusion implies that it is stationary. The oxygen flux from the gas phase onto the oxide surface is assumed fast compared to the flux of oxygen into the oxide, such that the oxygen supply from the gas is never rate limiting. Therefore there is an adsorbed layer of oxygen present on the oxide surface that is in chemical equilibrium with the gas phase, independent of the oxygen flux into the oxide. It is important to consider the charge state of oxygen species present on the oxide surface. For example, at room temperature oxygen primarily exists as a chemisorbed O^{-} species on nickel oxide [39] and as neutral O_2 on alumina [40]. We will consider cases with and without surface oxygen reduction. If reduced species do exist on the oxide surface then a second double layer will develop at the oxide-gas interface. We defer treating this second double layer until we have analyzed the oxide-metal interface. Below we describe the reaction rates and equilibrium conditions at the gas-oxide interface for both cases.

1. *No surface oxygen reduction*

If no reduced oxygen species exist on the oxide surface then the oxygen reduction and injection into the oxide must occur in a single step:

$$O_{\text{ads}}^{\times} + e' + V_A^{\bullet} \leftrightarrow A_A^{\times}. \tag{17}$$

The species $O_{\text{ads}}^{\times}$ is a charge-neutral oxygen adatom. The change in molar Gibbs free energy for the above reaction is

$$\Pi_{g/o} = -\bar{\mu}_v^{O} - \bar{\mu}_e^{O} - \mu_g, \tag{18}$$

remembering that the chemical potential of $O^{\times}_{\text{ads}}$ is equal to the chemical potential of oxygen in the gas, μ_g. The value of μ_g is given by $\mu_g = \mu_g^{\circ}(T) + \ln p_{O_2}^{1/2}$, where p_{O_2} is the partial pressure of O_2 in the gas. The temperature dependent standard state free energy of oxygen gas can be found in a thermochemical database [41]. The flux of vacancies and electrons at the gas-oxide interface due to the reduction reaction is taken to follow first-order reaction kinetics and is given by [42]

$$J_v = J_e = \kappa \Pi_{g/o}, \tag{19}$$

where κ is a temperature dependent rate constant. Equation (19) is valid for $|\Pi_{g/o}| \ll RT$. Equation (18) must be zero at equilibrium, which implies

$$\bar{\mu}_v^O + \bar{\mu}_e^O = -\mu_g \quad \text{at equilibrium.} \tag{20}$$

Therefore the bulk gas, oxide, and metal phases are at equilibrium when Eqs. (14), (15), and (20) are satisfied.

2. *Surface oxygen reduction*

If a reduced oxygen species does exist on the oxide surface then we assume the oxygen reduction and injection into the oxide occur in two steps, r_1 and r_2:

$$O^{\times}_{\text{ads}} + e' \overset{r_1}{\longleftrightarrow} O'_{\text{ads}},$$
$$O'_{\text{ads}} + V_A^{\bullet} \overset{r_2}{\longleftrightarrow} A_A^{\times};$$

where O'_{ads} is the reduced oxygen adatom. Note that these reactions sum to the reaction in Eq. (17). The surface molar density of reduced oxygen is denoted $c^{\mathcal{A}}$ (moles/m^2) and the associated surface charge density $\rho^{\mathcal{A}}$ is defined as $\rho^{\mathcal{A}} = -Fc^{\mathcal{A}}$.

The change in molar Gibbs free energy of each reaction step is

$$\Pi_{r1} = \bar{\mu}_{g^-} - \bar{\mu}_e^O - \mu_g, \tag{21}$$

$$\Pi_{r2} = -\bar{\mu}_v^O - \bar{\mu}_{g^-}, \tag{22}$$

where $\bar{\mu}_{g^-}$ is the electrochemical potential of the reduced oxygen adatoms and is treated as a constant here. We do not use the subscript o for $\bar{\mu}_{g^-}$ to avoid confusion with the notation for the electrochemical potential of oxygen in the oxide.

The reaction fluxes are again taken to follow first-order reaction kinetics and are given by

$$J_e = \kappa_{r_1} \Pi_{r_1}, \tag{23}$$

$$J_v = \kappa_{r_2} \Pi_{r_2}, \tag{24}$$

$$\frac{\partial \rho^{\mathcal{A}}}{\partial t} = \kappa_{r_2} \Pi_{r_2} - \kappa_{r_1} \Pi_{r_1}, \tag{25}$$

where κ_{r_1} and κ_{r_2} are the temperature dependent rate constants for r_1 and r_2. For simplicity we assume $\kappa_{r_1} = \kappa_{r_2}$. Equations (21) and (22) must be zero at equilibrium. If we substitute the gas-oxide equilibrium condition $-\mu_g - \bar{\mu}_e^O = \bar{\mu}_v^O$ from Eq. (20) into Eq. (21), then Eqs. (21) and (22) become equivalent and yield a single equation for the equilibrium condition of the reduced surface oxygen species:

$$\bar{\mu}_{g^-} = -\bar{\mu}_v^O \quad \text{at equilibrium.} \tag{26}$$

Since $\bar{\mu}_{g^-}$ is treated as a constant here for simplicity, Eqs. (21) and (22) will reach equilibrium due to shifts in the vacancy and electron electrochemical potentials at the gas-oxide interface. The presence of the reduced oxygen species does not change the equilibrium conditions for the bulk gas, oxide, and metal phases, which are still given by Eqs. (14), (15), and (20).

IV. OXIDE-METAL SHARP INTERFACE DESCRIPTION

We first treat the structural oxide-metal interface with a sharp interface approach in order to calculate the interfacial energy of the electrostatic double layer. The distribution of space charge at the interface in our model follows Gouy-Chapman theory, where the charged species obey a Boltzmann distribution and have a negligible size effect [43]. The Debye length L_D in the oxide and screening length L_S in the metal for our free energy formulation are derived in Appendix B and are given by

$$L_D = \left[\frac{F^2}{\varepsilon^O}\left(\frac{1}{B_v^O} + \frac{1}{B_e^O}\right)\right]^{-1/2}, \tag{27}$$

$$L_S = \left[\frac{F^2}{\varepsilon^M}\left(\frac{1}{B_v^M} + \frac{1}{B_e^M}\right)\right]^{-1/2}, \tag{28}$$

where ε^j is the permittivity of phase j. As discussed in Appendix B, in the dilute limit Eq. (27) agrees exactly with the expression given in Eq. (1), and Eq. (28) approaches the Thomas-Fermi screening length expected for a free electron gas as the anion concentration in the metal goes to zero.

In the sharp interface description there are discontinuities in the charge density and electric field, or equivalently the gradient of the electrostatic potential, at the structural interface. It is straightforward to calculate the magnitude of the space charge that accumulates at the interface to equilibrate the electrochemical potentials in the two materials, assuming the oxide is in the Wagner limit. To calculate the interfacial properties, we consider the oxide-metal interface to be at $x = 0$, with the oxide and metal extending to $x = -\infty$ and $x = \infty$, respectively. Since the absolute value of the electrostatic potential is arbitrary, we choose the value in the bulk oxide to be zero for convenience. The charge density profile, following Gouy-Chapman theory, is given by

$$\rho(x) = \begin{cases} \Lambda^O e^{x/L_D} & \text{for } x < 0, \\ \Lambda^M e^{-x/L_S} & \text{for } x > 0, \end{cases} \tag{29}$$

which has a jump discontinuity at $x = 0$. The constants Λ^O and Λ^M are the values of the charge density on either side of the oxide-metal interface. The total charge in either phase, σ^O and σ^M, can be calculated by integrating the charge density profiles:

$$\sigma^O = \lim_{x \to 0^-} \int_{-\infty}^{x} \rho(x')dx' = \Lambda^O L_D, \tag{30}$$

$$\sigma^M = \lim_{x \to 0^+} \int_{x}^{\infty} \rho(x')dx' = \Lambda^M L_S. \tag{31}$$

Charge neutrality implies that the total charge in the oxide-metal system, $\sigma^O + \sigma^M$, must be zero. We define the magnitude of the charge in either phase, $\sigma^{O/M}$, as

$$\sigma^{O/M} = |\sigma^O| = |\sigma^M|.$$

The condition of charge neutrality allows us to solve for Λ^M in terms of Λ^O, L_D, and L_S from Eqs. (30) and (31):

$$\Lambda^M = -\frac{L_D}{L_S}\Lambda^O.$$

We can solve for the electrostatic potential $\psi(x)$ in the system by integrating Gauss's law, Eq. (6), for the charge density profile in Eq. (29), with the boundary conditions

$$\lim_{x\to-\infty}\frac{\partial\psi}{\partial x} = \lim_{x\to\infty}\frac{\partial\psi}{\partial x} = 0,$$
$$\lim_{x\to-\infty}\psi = 0,$$
$$\lim_{x\to0^-}\psi = \lim_{x\to0^+}\psi,$$

where, again, the choice of $\psi = 0$ in the bulk oxide is arbitrary and chosen for convenience. The resulting expression for the electrostatic potential is

$$\psi(x) = \begin{cases} -\frac{\Lambda^O L_D^2}{\varepsilon^O}e^{x/L_D} & \text{for } x < 0, \\ -\frac{\Lambda^O L_D^2}{\varepsilon^O} + \frac{\Lambda^M L_S^2}{\varepsilon^M}(1 - e^{-x/L_S}) & \text{for } x \geqslant 0, \end{cases} \tag{32}$$

where $\psi(x)$ is continuous but $\partial\psi/\partial x$ is discontinuous at $x = 0$.

At equilibrium, the difference in the electrostatic potential between the oxide and metal phase is, by definition, the Galvani potential $\Delta\psi^\circ$. This allows us to solve for the magnitude of the interfacial charging σ^O and σ^M in terms of $\Delta\psi^\circ$ by considering the limits of Eq. (32):

$$\Delta\psi^\circ = [\lim_{x\to\infty}\psi(x)] - [\lim_{x\to-\infty}\psi(x)]$$
$$= -L_D\Lambda^O\left(\frac{L_D}{\varepsilon^O} + \frac{L_S}{\varepsilon^M}\right). \tag{33}$$

Note that the two definitions of the Galvani potential in Eqs. (16) and (33) are distinct but must be equal to the same value. We utilize Eq. (33) to solve for Λ^O and Λ^M in terms of $\Delta\psi^\circ$ and substitute the result into Eqs. (30) and (31) to find $\sigma^{O/M}$ as a function of $\Delta\psi^\circ$:

$$\sigma^{O/M} = \left|\left(\frac{L_D}{\varepsilon^O} + \frac{L_S}{\varepsilon^M}\right)^{-1}\Delta\psi^\circ\right|. \tag{34}$$

Our use of quadratic Gibbs free energy density functions results in a linear dependence of the surface charge on the Galvani potential, rather than $\sigma \propto \sinh(\Delta\psi^\circ)$ as is the case for an ideal solution model. In fact, Eq. (34) is the first-order expansion of the ideal solution expression for the interfacial charging of an electrostatic double layer [43].

We can derive the equilibrium electron and anion vacancy density profiles in the system by substituting the electrostatic potential profile given in Eq. (32) into the expression for the electrochemical potential given in Eq. (9). Electrochemical equilibrium requires

$$\bar{\mu}_i^O(x) = \bar{\mu}_i^M(x) = \text{constant}$$

for $i = v,e$. Applying the boundary conditions

$$\lim_{x\to-\infty}c_i^O = c_{eq}^O \quad \text{and} \quad \lim_{x\to\infty}c_i^M = c_{eq}^M$$

for $i = v,e$ and solving for the equilibrium electron and anion vacancy density profiles yields

$$c_i(x) = \begin{cases} c_{eq}^O - q_i\frac{F}{B_i^O}\psi(x) & \text{for } x < 0, \\ c_{eq}^M - q_i\frac{F}{B_i^M}[\psi(x) - \Delta\psi^\circ] & \text{for } x > 0, \end{cases} \tag{35}$$
$$\text{for } i = v,e,$$

where we have simplified the expression in Eq. (35) using the expression for the Galvani potential given in Eq. (33). Like $\rho(x)$ in Eq. (29), the electron and anion vacancy density profiles have jump discontinuities at $x = 0$.

Finally, we can calculate the electrostatic portion of the interfacial energy by integrating the free energy density over the oxide and metal using the charge densities and corresponding electrostatic potentials derived above (see Appendix C):

$$\gamma_\psi = \frac{1}{2}\left[\frac{\left(B_e^M - B_v^M\right)\left(\mu_{e,eq}^M + \mu_{v,eq}^M\right)}{F\left(B_e^M + B_v^M\right)} - \Delta\psi^\circ\right]\sigma^O. \tag{36}$$

Examining Eq. (36), the formation of the double layer will always decrease the total free energy of the system. The second term on the right-hand side of Eq. (36) is expected from electrocapillary theory, and alone would yield the well-known Lippmann equation $\sigma^O = -(\partial\gamma_\psi/\partial\Delta\psi^\circ)_{\mu_i}$ [44]. The first term on the right-hand side of Eq. (36) is a result of the free electron gas model and arises due to the difference in parabolic constants in the metal phase.

V. PHASE-FIELD MODEL

We now represent the structural oxide-metal phase boundary as a diffuse interface described by a phase-field parameter ϕ. The phase-field parameter ranges from 0 to 1, where $\phi = 0$ represents the oxide phase and $\phi = 1$ represents the metal phase. Bulk properties are interpolated smoothly across the diffuse interface by a common interpolation function $p(\phi) = \phi^3(10 - 15\phi + 6\phi^2)$ that satisfies $\partial p(\phi)/\partial\phi = 0$ in the bulk phases [45]. The value of $p(\phi)$ may be interpreted as the local volume fraction of the metal phase. The oxide-metal interface is considered a two-phase mixture, where the average molar density c_i in the mixture is the weighted average of the two phase densities [17]:

$$c_i = p(\phi)c_i^M + (1 - p(\phi))c_i^O \quad \text{for } i = e,v. \tag{37}$$

We assume that the phase compositions satisfy local electrochemical equilibrium in the two-phase mixture, following the standard approach for multi-component systems [46,47]. As both the phase-field interfacial thickness becomes small and the film thickness becomes large compared to the Debye length in the system, the phase-field model will approach the sharp interface description described in Sec. IV.

A. Free energy functional

The total free energy of the oxide-metal system is given by the free energy functional:

$$\mathcal{F}(\phi,c_v,c_e,\psi) = \int \left[G^{\phi} + G^{\rm tot} + \frac{1}{2}\psi\rho \right] dV, \tag{38}$$

that includes a phase-field, chemical, and electrostatic contribution.

The phase-field free energy density G^{ϕ} is the sum of a symmetric double well potential and a gradient energy penalty term, and is given by

$$G^{\phi} = \frac{\epsilon}{2}|\nabla\phi|^2 + A\,\phi^2[1-\phi]^2,$$

where ϵ is the gradient energy coefficient and A sets the height of the double well. The phase-field free energy density goes to zero in the bulk phases and sets the free energy penalty for components in the two-phase mixture at the interface. When the Galvani potential in the system is zero and there is no driving force for oxidation, no space charge develops in the system and the model reduces to a phase-field model of a phase transformation without charged species (see [17,48] for example). In this case, the two parameters ϵ and A completely determine the equilibrium thickness, ζ, and energy, γ_{ϕ}, of the oxide-metal structural interface:

$$\zeta = \sqrt{\frac{2\epsilon}{A}} \quad \text{and} \quad \gamma_{\phi} = \frac{\sqrt{\epsilon A}}{3\sqrt{2}}. \tag{39}$$

The second term in Eq. (38), $G^{\rm tot}$, is an interpolation of the chemical component of the Gibbs free energy densities of the pure phases given in Eqs. (10) and (11):

$$G^{\rm tot} = p(\phi)G^{M} + [1-p(\phi)]G^{O}. \tag{40}$$

The chemical free energy densities of the two phases in Eqs. (10) and (11) are expressed in terms of the individual phase densities c_e^O, c_e^M, c_v^O, and c_v^M. In order to express Eq. (40) in terms of the average molar densities c_v and c_e, defined in Eq. (37), we assume the local two-phase mixture is at electrochemical equilibrium. We do not include the equilibrium Galvani potential difference between the two phases in the two-phase mixture: $\psi^O(x) = \psi^M(x)$. Including this internal potential difference would imply a charged double layer at the interfaces within the two-phase mixture, and no double layer would develop across the diffuse interface. If one were interested in modeling an electrochemical interface using a grid spacing much larger than the electronic screening lengths in the materials of interest, then assuming an internal Galvani potential would be reasonable. Local electrochemical equilibrium within the two-phase mixture with no internal electrostatic potential difference implies, from Eq. (9),

$$\mu_{i,eq}^O + B_i^O\left(c_i^O - c_{eq}^O\right) = \mu_{i,eq}^M + B_i^M\left(c_i^M - c_{eq}^M\right) \quad \text{for } i = e,v. \tag{41}$$

The defect densities in each phase can be expressed as a function of ϕ and the average molar density c_i by solving the four equations given in Eqs. (37) and (41) for c_e^O, c_e^M, c_v^O, and c_v^M. Expressing Eq. (40) in terms of c_e and c_v, the total Gibbs free energy density can be simplified to

$$G^{\rm tot} = \sum_{i=v,e}\left[\mu_{i,eq}(c_i - c_{eq}) + \frac{1}{2}\frac{B_i^O B_i^M}{B_i}(c_i - c_{eq})^2 + \frac{F^2}{2}\frac{p(\phi)[1-p(\phi)]}{B_i}(\Delta\psi^{\circ})^2\right] + p(\phi)\Delta G^{\circ},$$

where

$$c_{eq} = p(\phi)c_{eq}^M + [1-p(\phi)]c_{eq}^O,$$
$$\mu_{i,eq} = \frac{[1-p(\phi)]B_i^M\mu_{i,eq}^O + p(\phi)B_i^O\mu_{i,eq}^M}{B_i},$$
$$B_i = [1-p(\phi)]B_i^M + p(\phi)B_i^O. \tag{42}$$

The ϕ dependent density profile c_{eq} can be interpreted as the average equilibrium defect density of the two-phase mixture, and would be the equilibrium defect density profile for $\Delta\psi^{\circ} = 0$. The phase-field dependent terms $\mu_{i,eq}$ and B_i are interpolated equilibrium chemical potentials and parabolic constants.

The third term in Eq. (38) is the electrostatic energy density in the system, where ψ is the electrostatic potential in the two-phase system and ρ is the charge density defined in Eq. (5). The electrostatic potential must satisfy Gauss's law everywhere:

$$-\nabla\cdot[\varepsilon(\phi)\,\boldsymbol{E}] = \nabla\cdot[\varepsilon(\phi)\,\nabla\psi] = -\rho(c_v,c_e),$$

where the permittivity $\varepsilon(\phi) = p(\phi)\varepsilon^M + [1-p(\phi)]\varepsilon^O$ is now treated as an explicit function of the phase-field variable ϕ and is an interpolation of the bulk values of the two phases. In reality the permittivity is depressed at the oxide-metal interface, but this is omitted in the present model for simplicity [49].

B. Phase-field oxide-metal interfacial energy

The interfacial energy per unit area in the phase-field model, denoted γ, is defined conventionally as

$$\mathcal{F} = V^O G^{\circ O} + V^M G^{\circ M} + \mathcal{A}\gamma, \tag{43}$$

where V^O and V^M are the volume of the oxide and metal phases and $\mathcal{A}$ is the area of the interface. The first two terms on the right-hand side of Eq. (43) are the free energies of the bulk oxide and metal phases at equilibrium, and the third term is the free energy of the interface. Remembering that $p(\phi)$ is the local volume fraction of the metal phase, $\Delta G^{\circ} \equiv G^{\circ M} - G^{\circ O}$, and the energy scale is set so that $G^{\circ O}$ is zero, the free energies of the bulk phases at equilibrium can be written

$$\begin{aligned} V^O G^{\circ O} + V^M G^{\circ M} &= \mathcal{A}\int\{[1-p(\phi)]G^{\circ O} + p(\phi)G^{\circ M}\}dx \\ &= \mathcal{A}\int p(\phi)\Delta G^{\circ}dx. \end{aligned} \tag{44}$$

Rewriting Eq. (38) as $\mathcal{F} = \mathcal{A}\int[G^{\phi} + G^{\rm tot} + \frac{1}{2}\psi\rho]dx$ and substituting it into the left-hand side of Eq. (43), we can use Eq. (43) along with Eq. (44) to solve for γ:

$$\gamma = \int\left[G^{\phi} + G^{\rm tot} + \frac{1}{2}\psi\rho - p(\phi)\Delta G^{\circ}\right]dV.$$

We show below that when the Debye length L_D and the screening length of the metal L_S are significantly larger than the structural interface thickness ζ, the interfacial energy approaches the sum of the structural and electrostatic interfacial energies given in Eqs. (36) and (39):

$$\gamma \to \gamma_\psi + \gamma_\phi \quad \text{for } \zeta/L_D \ll 1 \quad \text{and} \quad \zeta/L_S \ll 1. \tag{45}$$

C. Free energy minimization

The equilibrium solution of the oxide-metal system must minimize the free energy $\mathcal{F}(\phi, c_v, c_e, \psi)$ with respect the defect density, phase-field variable, and electrostatic potential fields. We cannot take functional derivatives of Eq. (38) with respect to ϕ, c_v, c_e, and ψ independently, however, because ψ is itself a functional of c_v and c_e by Gauss's law. Following the approach of Guyer *et al.* [22], we introduce a Lagrangian $\mathcal{L}$ to ensure that the solution satisfies Gauss's law without explicitly accounting for the dependence of ψ on c_v and c_e when taking the functional derivatives:

$$\mathcal{L} = \mathcal{F} - \int \lambda(\nabla \cdot [\varepsilon \nabla \psi] + \rho) dV,$$

where the Lagrange multiplier λ must be a field $\lambda(x)$ in order to satisfy Gauss's law across the system. The variations of $\mathcal{L}$ with respect to ϕ, c_v, c_e, and ψ are then

$$\frac{\delta \mathcal{L}}{\delta \phi} = \frac{\partial G^\phi}{\partial \phi} - \nabla \cdot \frac{\partial G^\phi}{\partial \nabla \phi} + \frac{\partial G^{\text{tot}}}{\partial \phi} + \frac{\partial \varepsilon}{\partial \phi} \nabla \lambda \cdot \nabla \psi, \tag{46}$$

$$\frac{\delta \mathcal{L}}{\delta c_i} = \frac{\partial G^{\text{tot}}}{\partial c_i} + \frac{1}{2} \psi F q_i - \lambda F q_i \qquad \text{for } i = v, e, \tag{47}$$

$$\frac{\delta \mathcal{L}}{\delta \psi} = \frac{1}{2}\rho - \nabla \cdot [\varepsilon \nabla \lambda]. \tag{48}$$

The variations with respect to the nonconserved fields ϕ and ψ must be zero and the variations with respect to the conserved density fields must be constant at equilibrium. By substituting Gauss's law into Eq. (48), we can see that Eq. (48) is zero only when $\lambda = -\frac{1}{2}\psi$, which reduces Eqs. (46) and (47) to

$$\frac{\delta \mathcal{L}}{\delta \phi} = \frac{\partial G^\phi}{\partial \phi} - \nabla \cdot \frac{\partial G^\phi}{\partial \nabla \phi} + \frac{\partial G^{\text{tot}}}{\partial \phi} - \frac{1}{2}\frac{\partial \varepsilon}{\partial \phi} |\nabla \psi|^2, \tag{49}$$

$$\frac{\delta \mathcal{L}}{\delta c_i} = \frac{\partial G^{\text{tot}}}{\partial c_i} + q_i F \psi = \bar{\mu}_i \qquad \text{for } i = v, e. \tag{50}$$

Equation (50) can be interpreted as the electrochemical potential of each species in the two-phase mixture. Considering Eq. (20), the gas-oxide-metal system is at equilibrium when $\bar{\mu}_v + \bar{\mu}_e = -\mu_g$ everywhere.

We formulate Allan-Cahn and Cahn-Hilliard type evolution equations for the nonconserved phase field and conserved defect density fields:

$$\frac{\partial \phi}{\partial t} = -M_\phi \frac{\delta \mathcal{L}}{\delta \phi}, \tag{51}$$

$$\frac{\partial c_i}{\partial t} = -\nabla \cdot \boldsymbol{J}_i = \nabla \cdot (M_i \nabla \bar{\mu}_i) \quad \text{for } i = v, e, \tag{52}$$

where M_v and M_e are the defect mobilities and M_ϕ is the phase-field mobility. We do not discuss the details of the mobilities here since they do not affect the equilibrium solutions. We make the simplifying assumption that the defect mobilities are constants so that they can be pulled outside of the divergence operator for computational efficiency.

TABLE I. Physical and phase-field parameters.

$\Delta\mu^\circ$	4×10^5 J/mol
c	9×10^4 mol/m^3
c_{eq}^O	0.0001 c
c_{eq}^M	0.999 c
T	1000 K
ε^M	ε_0
ε^O	$70\,\varepsilon_0$
$\Delta\psi^\circ$	0.05 V
ζ	$0.1\,L_D$
γ_ϕ	2×10^{-3} J/m^2

Values for the physical parameters used in the model, except when explicitly varied, are provided in Table I. These values result in a reasonable value of the difference in the two-phase equilibrium Gibbs free energy densities, ΔG°, of $\sim 7 \times 10^5$ J/mol for an oxide-metal system [7]. The permittivity of the oxide is chosen as an approximation for the high-temperature permittivity of alumina [50,51]. The permittivity of the metal is the real part of the static permittivity of a free electron gas [52]. The dependence of the model on the equilibrium defect densities c_{eq}^O and c_{eq}^M as well as the structural interface thickness ζ is discussed below.

D. Nondimensionalization

For numerical purposes, the model is scaled by the Debye length L_D, chemical diffusion coefficient of anion vacancies in the oxide D_v, molar density of the oxide c, and temperature T. The nondimensionalized physical parameters are indicated with a tilde and given by

$$\tilde{x} = \frac{x}{L_D}, \quad \tilde{c} = \frac{c}{\text{c}}, \quad \tilde{t} = \frac{t\,D_v}{L_D^2}, \quad \tilde{\kappa} = \frac{\kappa RT L_D}{\text{c} D_v},$$

$$\tilde{G} = \frac{G L_D^3}{k_B T}, \quad \tilde{B} = \frac{B\text{c}^2 L_D^3}{k_B T}, \quad \tilde{\epsilon} = \frac{\epsilon\, L_D}{k_B T}, \quad \tilde{A} = \frac{A\, L_D^3}{k_B T},$$

$$\tilde{\varepsilon} = \frac{\varepsilon RT L_D N_A}{F^2}, \quad \tilde{\rho} = \frac{\rho L_D^3 N_A}{F}, \quad \tilde{\mu} = \frac{\mu \text{c} L_D^3}{k_B T},$$

$$\tilde{\psi} = \frac{\psi F}{RT}, \quad \tilde{\text{c}} = \text{c} L_D^3 N_A, \quad \tilde{M}_e = \frac{M_e k_B T}{D_v \text{c}^2 L_D^3},$$

$$\tilde{M}_v = \frac{M_v k_B T}{D_v \text{c}^2 L_D^3}, \quad \tilde{M}_\phi = \frac{M_\phi k_B T}{D_v L_D}.$$

From this point forward we drop the tildes and take all physical variables to be in their nondimensional form. The evolution equations (51) and (52) and Poisson's equation are cast in dimensionless form and solved below. The nondimensionalized evolution equations are provided in Appendix D.

VI. NUMERICAL METHODS AND CONVERGENCE

The nondimensionalized forms of the evolution equations (D1), (D2), and (D3) are solved with an explicit Euler scheme using second-order finite differences on a uniform grid. The sharp gas-oxide interface and the center of mass of the metal

are located at the left and right boundary points, $x = 0$ and $x = x_r$. The system is considered symmetric about $x = x_r$, which implies the metal is being oxidized from both sides and another oxide-gas interface exists at $x = 2x_r$. Symmetry then implies the following boundary conditions at $x = x_r$:

$$\boldsymbol{J}_v|_{x=x_r} = \boldsymbol{J}_e|_{x=x_r} = 0,$$
$$\nabla\psi|_{x=x_r} = 0.$$

A. Gas-oxide interfacial boundary conditions

The oxygen chemical potential in the gas, μ_g, is set to satisfy Eq. (20) in all simulations. The value of the electrochemical potential of the reduced adsorbed oxygen species, $\bar{\mu}_{g^-}$, is discussed below. In the first two sections of results, Secs. VII A and VII B, no adsorbed oxygen reduction is permitted. This allows the oxide-metal interface to be studied without the presence of another double layer at the gas-oxide interface. In this case, because μ_g is set to satisfy Eq. (20), the boundary conditions for the defect fluxes at the gas-oxide interface according to Eq. (19) are given by

$$\boldsymbol{J}_v|_{x=0} = \boldsymbol{J}_e|_{x=o} = 0.$$

If oxygen reduction is permitted, as in Sec. VII C, then the boundary conditions for the defect fluxes at the gas-oxide interface are given by Eqs. (23) and (24). In this case as the system evolves the oxide surface will charge until Eq. (26) is satisfied, where the equilibrium value of the surface charge density $\rho^{\mathcal{A}}$ is a function of $\bar{\mu}_{g^-}$.

B. Electrostatics

1. No surface oxygen reduction

If no charge exists on the oxide surface then the boundary conditions are such that charge is conserved over the domain $0 \leqslant x \leqslant x_r$. The electrostatic potential and electric field are computed at each time step by integrating Gauss's law using the trapezoidal rule with the boundary conditions $\psi(x=0)=0$ and $\boldsymbol{E}(x=0)\cdot\hat{\boldsymbol{x}} = 0$:

$$\boldsymbol{E}(x)\cdot\hat{\boldsymbol{x}} = \frac{1}{\varepsilon(x)}\int_0^x \rho(x')\,dx', \tag{53}$$

$$\psi(x) = -\int_0^x \boldsymbol{E}(x')\cdot\hat{\boldsymbol{x}}\,dx', \tag{54}$$

which ensures that the value of $\boldsymbol{E}(x)\cdot\hat{\boldsymbol{x}}$ will be zero at $x = x_r$ if the evolution equations are accurate to at least second order.

2. Surface oxygen reduction

If surface oxygen reduction is included in the model, then the charged layer on the oxide surface invalidates the boundary condition $\boldsymbol{E}(x=0)\cdot\hat{\boldsymbol{x}} = 0$. We assume the thickness of the adsorbed surface layer, l, is short compared to other physical length scales in the system. In this case the boundary conditions for the electric field and electrostatic potential at $x = 0$ can be found by integrating Gauss's law from $x = -l$ to $x = 0$ in the limit $l \to 0$, assuming constant charge density within the layer:

$$\boldsymbol{E}(x=0)\cdot\hat{\boldsymbol{x}} = \frac{\rho^{\mathcal{A}}}{\varepsilon^{\mathcal{A}}},$$
$$\psi(x=0) = 0,$$

where $\varepsilon^{\mathcal{A}}$ is the permittivity of the reduced oxygen layer. So the charged surface layer does not introduce a jump in the electrostatic potential at the gas-oxide interface in the limit $l \to 0$, but does introduce a jump in the gradient of the electrostatic potential.

The electric field and electrostatic potential within the oxide and metal phases are still calculated according to Eqs. (53) and (54), except that $x = -l$ is the lower bound of the integral rather than $x = 0$.

C. Metal screening length relaxation

For protective oxide phases, the Debye length is at least an order of magnitude larger than the structural oxide-metal interface assuming a reasonable structural interface thickness of around 0.5 nm. A typical Thomas-Fermi screening length in a metal, however, tends to be on the order of 0.5 Å. This requires the structural interface be ~0.05 Å in order to uncouple the electrostatic and structural interfacial properties, which is currently computationally unfeasible since we want to model oxide scales on the order of a few Debye lengths in thickness. For this reason we are motivated to relax the screening length in the metal to make the problem more tractable. We introduce a relaxation factor α that scales the permittivity and the parabolic coefficients of the chemical free energy density of the metal in such a way that the screening length L_S increases but the magnitudes of the interfacial charge $\sigma^{O/M}$ and electrostatic interfacial energy γ_ψ, given in Eqs. (34) and (36), are unchanged:

$$B_v^M \to \alpha B_v^M, \quad B_e^M \to \alpha B_e^M, \quad \epsilon^M \to \alpha\epsilon^M. \tag{55}$$

The above scaling increases L_S by a factor of α but leaves the defect structure in the oxide phase unchanged. It is unhelpful to relax L_S larger than L_D, as the maximum structural interface thickness will then be limited by L_D. Relaxing L_S has the disadvantage that the domain size must be increased to ensure that the metal thickness remains much greater than L_S, but this disadvantage is far outweighed by the computational gains from increasing the grid spacing. The equilibrium charge distribution and electrostatic potential profiles for several values of α are shown in Fig. 2, demonstrating that the defect structure profiles and electrostatics in the oxide are unaffected by relaxing the metal's screening length. In all subsequent results, the screening length is relaxed to the Debye length by setting $\alpha = L_D/L_S$.

In Fig. 2, the ratio of the phase-field interface thickness to the metal's screening length, ζ/L_S, was set to 0.1. This choice was made by testing the convergence of the phase-field model to the sharp interface description as a function of ζ/L_D. Charge distributions near the oxide-metal interface for five values of ζ/L_D are shown in Fig. 3. The correspondence between the charge distribution in the phase-field model and the sharp interface double layer described by Eq. (29) becomes better as ζ/L_D decreases. In order to measure how well the phase-field model captures the sharp interface description, we calculate the error in Eq. (45), which is a measure of how decoupled the structural interfacial free energy and the electrostatic interfacial free energy are. The error in Eq. (45) is plotted as a function of ζ/L_D in Fig. 4. Equation (45) is satisfied within 0.5% for $\zeta/L_D = 0.1$, which we choose as

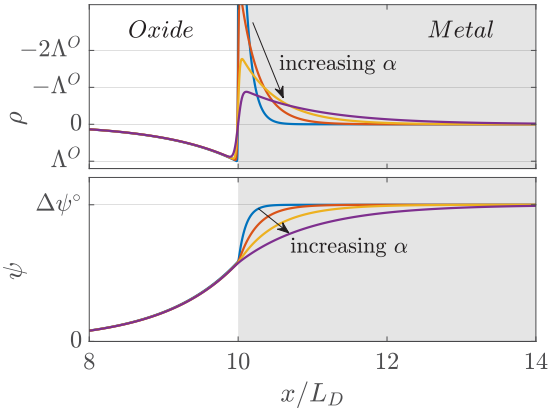

FIG. 2. Equilibrium charge distributions and electrostatic potentials for four values of α that set $L_S/L_D = 1$, 0.5, 0.25, and 0.1. The ratio of ζ to L_S is 0.1 in all cases. The charge distribution and electrostatic potential in the oxide are unaffected by the relaxation of the metal's screening length.

an acceptable value for accurately reproducing the the sharp interface description.

VII. RESULTS AND DISCUSSION

A. Wagner limit

The Debye length in the oxide is ~5.5 nm for the parameters listed in Table I. The equilibrium defect density profiles, along with the average two-phase equilibrium density c_{eq} defined in Eq. (42), for an oxide film of thickness $L = 10L_D$ are plotted in Fig. 5. The oxygen vacancy and electron densities go from 0.0001 in the oxide to 0.999 to the metal. This makes it difficult to see the shifts in the defect profiles at the interface because they are small relative to the overall density change across the interface. Since c_{eq} is the equilibrium density profile across the interface for $\Delta\psi^\circ = 0$, we are really interested in the deviations of c_a and c_e relative to c_{eq} for $\Delta\psi^\circ \neq 0$, which will show the changes in c_a and c_e from c_{eq} at the interface due to the formation of the double layer.

The deviations of the anion vacancy and electron density relative to c_{eq} for $L = 10L_D$, as well as the corresponding charge density and electrostatic potential, for the same

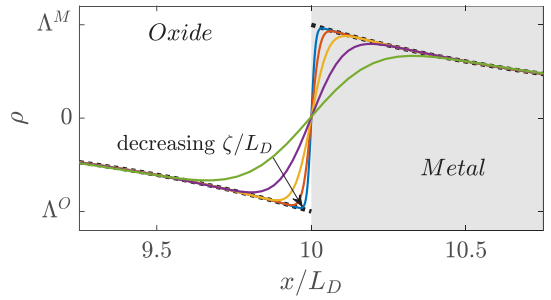

FIG. 3. Charge distribution near the oxide-metal interface for $\zeta/L_D = 0.4$, 0.2, 0.1, 0.05, and 0.025. The dashed black lines are the sharp interface solutions given in Eq. (29). The screening length in the metal is relaxed to L_D. The white and light gray regions indicate the oxide and metal, respectively.

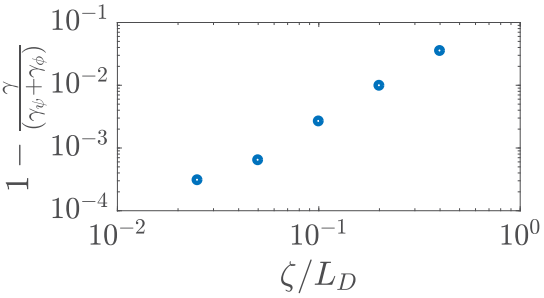

FIG. 4. Error in Eq. (45) as a function of ζ/L_D. The error converges with $(\zeta/L_D)^2$ until $\zeta/L_D \approx 0.25$, at which point the error due to the grid spacing becomes significant. For $\zeta/L_D = 0.1$, Eq. (45) is satisfied within 0.5%.

simulation shown in Fig. 5 are shown in the left panel of Fig. 6. As seen in Fig. 5, both defect densities approach c_{eq} in the bulk phases, which are at equilibrium once the Galvani potential difference has established across the interface. Near the interface, the defect densities approach the interfacial values of the sharp interface density profiles given in Eq. (35), which are indicated in Fig. 6 by the dashed horizontal lines in the defect density plots.

The defect density and electrostatic potential profiles will always be exponential in the thick-film limit. However, the interfacial values of the defect densities relative to the two-phase equilibrium defect densities will be a function of the two-phase equilibrium defect densities according to Eq. (35). To visualize how the interfacial values of the defect densities change as a function of the two-phase equilibrium defect densities, the shift in the equilibrium oxygen vacancy density from Eq. (35) relative to c_{eq}^O at $x = L$ as a function of the equilibrium defect density in the oxide, $[c_v(x = L) - c_{eq}^O]/c_{eq}^O$, is plotted in Fig. 7. As $c_{eq}^O \to 0$, the value of $[c_v(x = L) - c_{eq}^O]/c_{eq}^O$ approaches a constant value for a given value of $\Delta\psi^\circ$. This is because as $c_{eq}^O \to 0$, $B_v^O = B_e^O \to \infty$, which decreases the equilibrium deviations from c_{eq}^O as c_{eq}^O becomes small. The

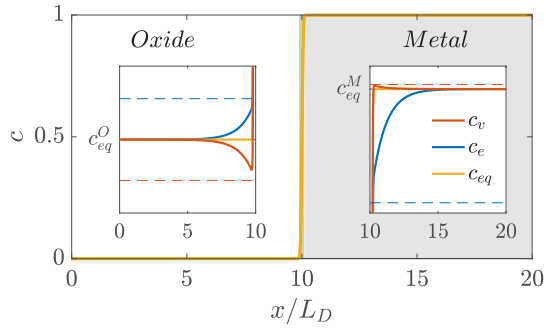

FIG. 5. Equilibrium defect density profiles across the oxide-metal interface for $L = 10L_D$, as well as the average two-phase equilibrium density c_{eq} given in Eq. (42). The horizontal dashed lines indicate the interfacial values of the defect concentrations in the sharp interface treatment, given in Eq. (35). The defect densities are at equilibrium at c_{eq} in the bulk phases once the Galvani potential difference has developed across the interface, but deviate from c_{eq} near the interface for $\Delta\psi^\circ \neq 0$ due to the double layer formation. The deviations of c_v and c_e from c_{eq} for this simulation are plotted in Fig. 6.

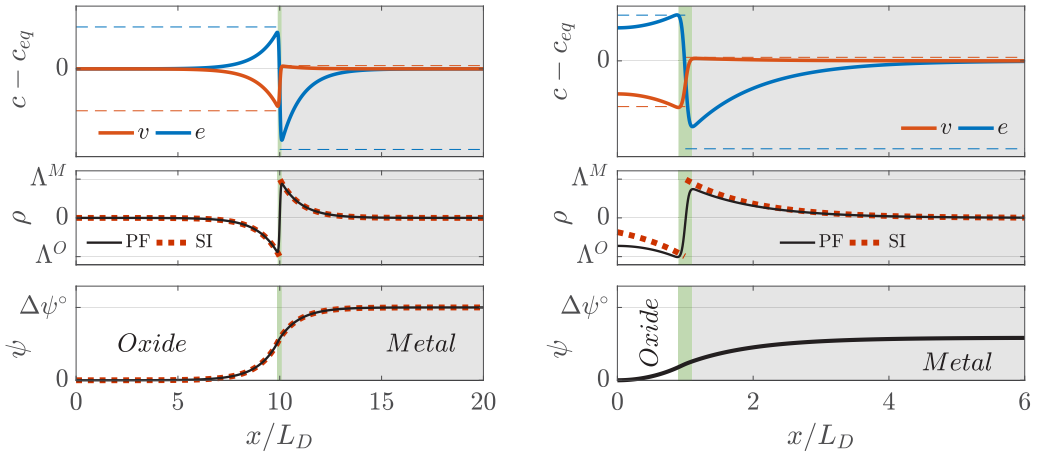

FIG. 6. The deviations of the anion vacancy and electron density relative to c_{eq} (see Fig. 5), charge density, and electrostatic potential profiles for an equilibrium oxide-metal interface with $L = 10L_D$ (left) and $L = L_D$ (right). The left figure is the same simulation as Fig. 5. The horizontal dashed lines in the defect density plots indicate the oxide-metal interfacial values of the defect concentrations in the sharp interface treatment, given in Eq. (35). Sharp interface (SI) profiles for the charge density and electrostatic potential from Eqs. (29) and (32) are also plotted with the phase-field (PF) results. The interfacial region defined by $L - \zeta < x < L + \zeta$ is shaded in light green.

value of $[c_v(x = L) - c^O_{eq}]/c^O_{eq}$ is weakly dependent on c^M_{eq} and the dependance weakens as $1 - c^M_{eq} \to 0$, being nearly independent of c^M_{eq} for $1 - c^M_{eq} < 10^{-3}$ as evident in Fig. 7. This is advantageous for the model because it demonstrates that the equilibrium defect density in the metal does not strongly affect the defect structure in the oxide.

The two defect structures contribute equally to the electronic screening in the oxide phase as seen in the symmetric deviations of c_v and c_e from c_{eq} in Figs. 5 and 6. This is because the density of the anion and cation sublattices are equal in our model, which leads to both defects having the same parabolic constants in the oxide according to Eq. (A1). In the metal, however, the free electron gas is nearly exclusively responsible for electronic screening as expected from Eq. (B2), unlike in previous phase-field models of oxide-metal interfaces [24,25].

The charge distribution and electrostatic potential shown in Fig. 6 from the phase-field simulation show excellent agreement with the sharp interface description given in Eqs. (29) and (32). This demonstrates that for a typical oxide-metal system, where the Debye length is an order of magnitude larger than the structural interface, the electrostatic and structural

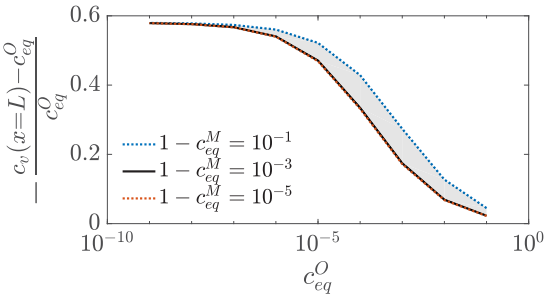

FIG. 7. The thick-film limit of the deviation of the equilibrium oxygen vacancy density in the oxide at the oxide-metal interface ($x = L$) from Eq. (35) relative to c^O_{eq} as a function of the equilibrium defect density in the oxide. Three values of the equilibrium defect density in the metal are plotted.

interfaces can be treated effectively as independent when the screening length in the metal is relaxed. This is advantageous because, although we cannot derive a closed-form solution for γ in the phase-field model, we can accurately predict it given the large difference in interfacial length scales.

B. Below the Wagner limit

The deviations in the equilibrium defect density profiles from c_{eq}, charge density, and electrostatic potential for a thin oxide film are shown in the right panel of Fig. 6. Note that the interfacial region in the thin-film limit looks larger than that in in the Wagner limit due to the smaller domain size shown. Unlike in the Wagner limit, all of the oxide is charged at equilibrium when the film is thin, which invalidates the oxide-metal equilibrium equations given in Sec. III B because the oxide can no longer be assumed charge neutral. Therefore the equilibrium potential difference between the two phases will not equilibrate to the Galvani potential defined in Eq. (16), as seen in Fig. 6. The thin oxide layer is unable to accommodate enough charge to lower the electrochemical potential of charged defects in the metal by the difference in two-phase equilibrium chemical potential levels. To illustrate this, we plot the equilibrium electrostatic potential difference between the two phases, $\Delta\psi_{eq} = \psi|_{x=x_r} - \psi|_{x=0}$, and the interfacial charge σ as a function of L/L_D in Fig. 8. Following Guyer *et al.* we define the interfacial charge in the phase-field simulation as

$$\sigma = \int p(\phi)\rho \, dV, \tag{56}$$

where we have chosen to integrate over the metal so that σ is positive. Charge conservation ensures that integrating over the oxide, $\sigma = \int [1 - p(\phi)]\rho \, dV$, will yield the same magnitude result as Eq. (56) but with opposite sign; therefore the choice is arbitrary. As expected from the sharp interface treatment, as L/L_D becomes large $\Delta\psi_{eq}$ and σ approach $\Delta\psi^\circ$ and $\sigma^{O/M}$, respectively. Below approximately $L/L_D = 1$, $\Delta\psi_{eq}$ and σ begin to decrease towards zero with decreasing oxide thickness proportional to $\exp(L/L_D)$. Since $\Delta\psi_{eq}$ is a

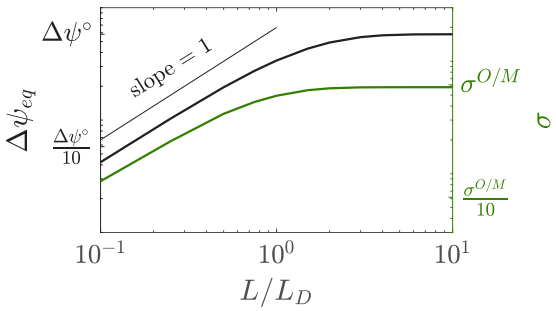

FIG. 8. Log-log plot of the equilibrium electrostatic potential (black) and interfacial charge (green) across the oxide-metal interface as a function of L/L_D. As the film becomes thick compared to the Debye length, $\Delta\psi_{eq}$ approaches $\Delta\psi^\circ$ and σ approaches $\sigma^{O/M}$ defined in Eq. (34). As L becomes small compared to the Debye length, both $\Delta\psi_{eq}$ and σ decay to zero as $\exp(L/L_D)$.

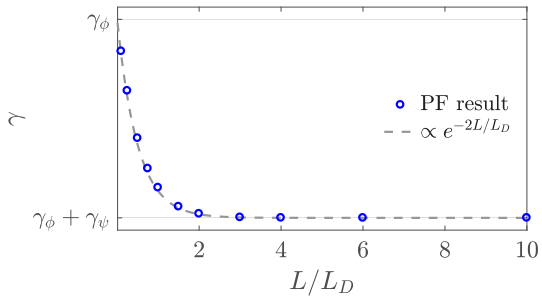

FIG. 10. Equilibrium interfacial energy γ as a function of L/L_D. When the film is thin, the electrostatic interface is unable to fully develop and γ approaches the structural interfacial energy γ_ϕ. As the film thickens, the electrostatic interface develops and γ approaches the sum of the structural and electrostatic interfacial energies $\gamma_\phi + \gamma_\psi$. The interfacial energy decays as $\gamma \propto \exp(-2L/L_D)$.

measure of the system's ability to lower the Fermi level in the two-phase system to the equilibrium electron chemical potential in the oxide, this indicates that the Fermi level at the gas-oxide interface will be higher for thin oxide films. This is confirmed in Fig. 9, where the equilibrium value of $\bar{\mu}_e$ at $x = 0$ is plotted as a function of L/L_D. For large L/L_D, $\bar{\mu}_e|_{x=0}$ approaches $\mu^O_{e,eq}$ as expected for a thick oxide film. As L/L_D becomes small, $\bar{\mu}_e|_{x=0}$ approaches $\mu^M_{e,eq}$. So as a thin oxide film transitions into the Wagner regime, the Fermi level at the gas-oxide interface decays approximately exponentially from $\mu^M_{e,eq}$ to $\mu^O_{e,eq}$ as the thickness of the film is increased, with a characteristic length scale of L_D. This change in Fermi level at the gas-oxide interface does not affect the equilibrium oxygen chemical potential in the gas, given in Eq. (20), because the equilibrium electrochemical potential of oxygen vacancies at the gas-oxide interface is lowered by an equal amount. However it does increase the driving force for surface oxygen reduction, Π_{r1} defined in Eq. (21), which we discuss in Sec. VII C.

The equilibrium oxygen chemical potential required in the gas is not affected by the shift in Fermi level for thin films; however it does decrease slightly in the thin film regime. This is due to the increase in interfacial energy γ of the oxide-metal interface as the film becomes thin, which is plotted in Fig. 10. As seen in the figure, γ is proportional to $\exp(-2L/L_D)$ and decays from the structural interface value γ_ϕ to the thick-film limit $\gamma_\phi + \gamma_\psi$ as the film thickness becomes large compared to L_D. The $\exp(-2L/L_D)$ decay is the result of both the electrostatic potential difference and interfacial charge increasing as $\exp(L/L_D)$ to their thick film limits, as seen in Fig. 8, which determine the electrostatic free energy of the charge distribution. The magnitude of the transition is determined by the relative sizes of the two interfacial energies given in Eqs. (36) and (39). This decrease in interfacial energy with increasing L implies that the thin oxide film has a lower equilibrium value of μ_g than the thick film limit $\mu_g = -\mu^O_{v,eq} - \mu^O_{e,eq}$. The additional driving force for oxidation due to this effect will in general be small compared to the bulk driving force of oxidation at realistic oxygen partial pressures, which is large. This implies that the double layer will mainly affect the oxide growth law through its influence on the defect densities and electric field in the oxide.

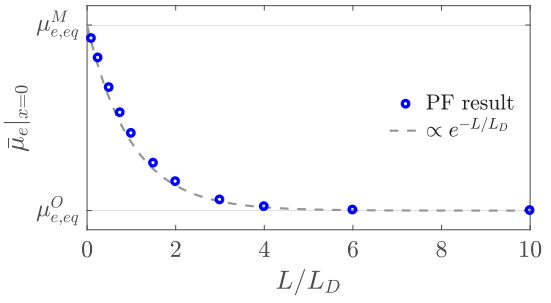

FIG. 9. Equilibrium electrochemical potential of electrons at the gas-oxide metal interface as a function of L/L_D. When the oxide film is thin compared to the Debye length, the electrochemical potential of electrons at the gas-oxide interface is equal to $\mu^M_{e,eq}$. As the film thickens, $\bar{\mu}_e|_{x=0}$ approaches $\mu^O_{e,eq}$, indicating that the bulk oxide is nearly charge free and the conditions of bulk phase equilibrium given in Sec. III B are satisfied.

C. Surface oxygen reduction

To investigate the effect of adsorbed surface oxygen reduction in the system we include the surface reduction reaction as described in Sec. III C 2. Phase-field results for the equilibrium surface charge density $\rho^{\mathcal{A}}$ as a function of both the electrochemical potential of the O^- adatoms $\bar{\mu}_{g^-}$ and the oxide thickness are plotted in Fig. 11. The value of $\bar{\mu}_{g^-}$ is plotted relative to $\mu^O_{v,eq}$ because in the Wagner limit when $\bar{\mu}_{g^-} = -\mu^O_{v,eq}$ no surface oxygen reduction will occur at three-phase equilibrium. This is evident from Eq. (26) because the equilibrium value of $\bar{\mu}^O_v$ will approach $\mu^O_{v,eq}$ in the Wagner limit, and is confirmed in Fig. 11 by the fact that $\rho^{\mathcal{A}}$ goes to zero as $\bar{\mu}_{g^-} + \mu^O_{v,eq}$ goes to zero and L/L_D becomes large.

In Fig. 11 the magnitude of $\rho^{\mathcal{A}}$ increases linearly as $\bar{\mu}_{g^-}$ decreases, whereas it increases exponentially as L/L_D decreases. The linear relationship between $\rho^{\mathcal{A}}$ and $\bar{\mu}_{g^-}$ is a result of the quadratic free energy densities, having the same origin as the linear dependence of the surface charge $\sigma^{O/M}$ on the Galvani potential in Eq. (34). The exponential dependence of $\rho^{\mathcal{A}}$ on L/L_D is related to the exponential dependence of

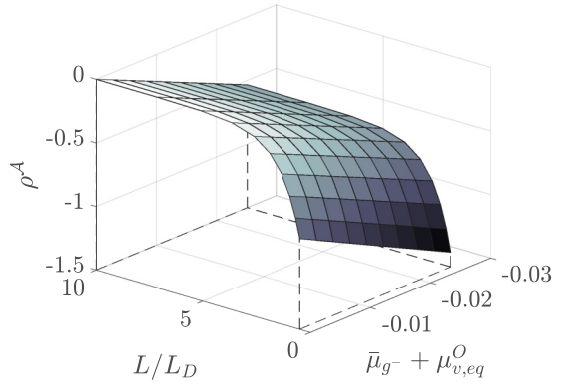

FIG. 11. The phase-field value of the equilibrium surface charge density $\rho^{\mathcal{A}}$ as a function of both the electrochemical potential of the O^- adatoms, $\bar{\mu}_{g^-}$, and the oxide thickness. The value of $\bar{\mu}_{g^-}$ is plotted relative to $\mu^O_{v,eq}$ because in the Wagner limit when $\bar{\mu}_{g^-} = -\mu^O_{v,eq}$ no surface oxygen reduction will occur at three-phase equilibrium, which is demonstrated by the fact that $\rho^{\mathcal{A}}$ goes to zero as $\bar{\mu}_{g^-} + \mu^O_{v,eq}$ goes to zero and L/L_D becomes large.

the vacancy and electron electrochemical potential at $x = 0$ on L/L_D, as demonstrated in Fig. 9.

To visualize the defect density and electrostatic profiles in the oxide with reduced oxygen adatoms present, we plot the equilibrium defect density profiles, charge density, and electrostatic potential for $L = 10L_D$ and $L = L_D$ in the left and right panels, respectively, of Fig. 12. These simulations are equivalent to those in the left and right panels of Fig. 6 except for the presence of the charged surface layer of infinitesimal thickness l, which is shown schematically in the figures. The electrochemical potential of the reduced oxygen adatoms, $\bar{\mu}_{g^-}$, is set to $\mu^O_{v,eq} - 0.02$ eV/mole. This value is chosen in light of Fig. 11 so that both the value of $\bar{\mu}_{g^-}$ and the film thickness have the same order of magnitude effect on the equilibrium value of the surface charge $\rho^{\mathcal{A}}$. These simulations are initialized with $\rho^{\mathcal{A}} = 0$, which then decreases according the Eq. (25) until equilibrium is reached. This leads to the formation of an additional double layer and associated electrostatic potential gradient at the gas-oxide interface. As discussed above, in the limit of $l \to 0$, the drop in ψ across the surface layer goes to zero, but the gradient of ψ at $x = 0$ is nonzero, unlike in the case of no surface oxygen reduction.

In the thick-film limit, shown in the left panel of Fig. 12, the double layers at the gas-oxide and oxide-metal interfaces are nearly independent. In this case, the charge distribution and electrostatic potential difference across the oxide-metal interface still agree with the sharp interface treatment. The double layer at the gas-oxide interface raises the electrostatic potential in both the oxide and metal relative to the gas and the magnitude of this shift is proportional to chemical potential of the O^- adatoms. However, because the gas-oxide double layer shifts ψ in both the oxide and metal phases, the oxide-metal equilibrium conditions given in Eqs. (14) and (15) still hold.

For a film of thickness $L = L_D$, shown in the right panel of Fig. 12, the double layers at the gas-oxide and oxide-metal interfaces cannot be considered independently. In this case, electrons from the metal will also contribute to oxygen reduction at the gas-oxide interface which leads to a larger surface charge density $\rho^{\mathcal{A}}$ than that in the thick-film limit shown in the left panel of Fig. 12. From the charge density profile for the thin film in Fig. 12, we see that the metal is more negatively charged than we would expect from the sharp interface model of the single oxide-metal interface. Again, this is because electrons from the metal are being transferred to both the oxide and surface layer. This is the opposite result of what happens when no surface charging is permitted as in Fig. 6, which is discussed above.

In the thin-film limit with surface charging, the defect density, charge density, and electrostatic potential profiles all become approximately linear. This is because the film thickness is on the order of the screening length and the

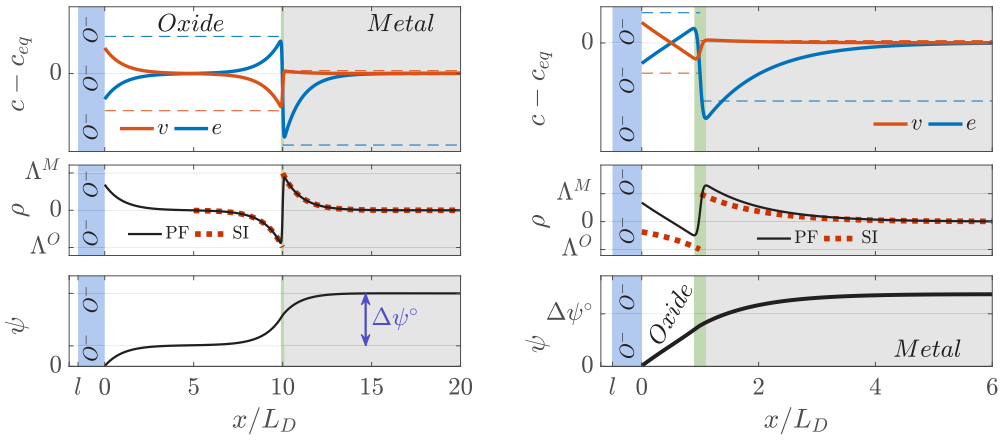

FIG. 12. The deviations of the anion vacancy and electron density relative to c_{eq} (see Fig. 5), and electrostatic potential profiles for an equilibrium gas-oxide-metal system $L = 10L_D$ (left) and $L = L_D$ (right), with a layer of reduced oxygen on the surface. The horizontal dashed lines in the defect density plots indicate the interfacial values of the defect concentrations in the sharp interface treatment, given in Eq. (35). The sharp interface (SI) profile for the charge density at the oxide-metal interface from Eq. (29) is also plotted with the phase-field (PF) results. The sharp interface model gives a poor description of the state of the oxide in the thin-film limit (right), as expected. The interfacial region defined by $L - \zeta < x < L + \zeta$ is shaded in light green. The layer of reduced oxygen on the oxide surface is shown schematically as the light blue region, where the thickness l is exaggerated to make it visible. The electrostatic potential drop between the bulk oxide and metal in the thick-film limit (left), or Galvani potential, is highlighted and equal to $\Delta\psi^\circ$.

exponential decay e^{-x/L_D} appears roughly linear for $x/L_D \ll 1$. The constant electrostatic potential profile in the oxide is familiar from the potential profiles assumed in other theories of thin film oxide growth such as the point defect model [53] and Cabrera-Mott theory [13]. This is not the case when no surface charging is permitted. The reason for this is that the boundary condition $\boldsymbol{E}(x=0)\cdot\hat{\boldsymbol{x}}=0$ constrains the equilibrium gradients of the defect and charge densities at $x=0$ to all be zero, which is evident in Fig. 6.

VIII. CONCLUSIONS

We have developed a phase-field model of an oxide-metal interface in a gas-oxide-metal system and studied its equilibrium behavior. The model includes a hybrid ideal solution and free electron gas description of the bulk thermodynamics, and Poisson's equation to describe the electrostatics. The phase-field method achieves an accurate representation of a Gouy-Chapman double layer, derived herein using a sharp interface description, when the electronic screening lengths in both phases are significantly larger than the length scale of the structural interface. While the screening length in protective oxide phases satisfies this condition, the screening length in a metal is generally on the same order of magnitude or smaller than an oxide-metal structural interface width, which makes it difficult to model the double layer without using a computationally intractable structural interface width. However, we have shown that the screening length in the metal can be relaxed without modifying the defect profiles, interfacial energy, or Debye length in the oxide. This allows for the maximum structural interface width to be set by the Debye length rather than the metal's screening length. We have not derived an analytical expression for the interfacial energy in the phase-field model, but show that it is accurately described by the sum of independent structural and electrostatic interfacial energies for $\zeta/L_D \lesssim 0.1$, the ratio of the structural interface width to the Debye length.

The phase-field simulations show that an oxide film of thickness on the order of the Debye length or smaller is unable to establish the equilibrium Galvani potential expected between the bulk oxide and metal phases in the thick-film limit, which results in the oxide being charged throughout. For the defect structure considered above this leads to a decrease in the ionic defect concentration; however, a number of possible charge distributions across the oxide are possible depending on the relative kinetics and energies of transfer of the charged defects at the oxide-metal and gas-oxide interfaces [10]. This space charge can either inhibit or enhance the oxidation rate depending on whether it has the same or opposite sign as the rate limiting species, respectively [21]. As the oxide film becomes thin relative to the Debye length, an increase in the oxide's Fermi level increases the driving force for surface oxygen reduction, which can modify the shape of the electric field in the oxide by changing the magnitude of the surface charge on the gas-oxide interface.

The present study is motivated by the desire to model oxide films during growth. Thermodynamic assessments show that oxide-metal systems of interest can only be at thermodynamic equilibrium with oxygen gas for extremely low oxygen partial pressures [8]. Therefore, as discussed above, protective oxide phases inhibit corrosion kinetically rather than thermodynamically. Solving for the equilibrium solution to the oxide-metal system is useful in that it allows us to quantitatively study how the phase-field formulation couples to the electrostatic double layer, which would not be possible in a nonequilibrium simulation and which has not been done in the previous phase-field models of oxidation.

ACKNOWLEDGMENTS

This work was supported by the Office of Naval Research MURI Grant No. N00014-14-1-0675. Calculations were performed using the HPCMP facilities at the Navy DoD Supercomputing Resource Center. We would like to thank S. O. Poulsen for useful comments on the manuscript.

APPENDIX A: GIBBS FREE ENERGY COEFFICIENTS

The Gibbs free energy coefficients in Eq. (8) written as functions of the standard state chemical potentials and two-phase equilibrium concentrations are

$$\mu^O_{i,eq} = \mu^{\circ O}_{\{i\}} + RT\ln\frac{c^O_{eq}}{\mathrm{C}} - RT\ln\frac{\mathrm{C}-c^O_{eq}}{\mathrm{C}} \quad \text{for } i=v,e,$$

$$\mu^M_{v,eq} = -\mu^{\circ M}_{\{a\}} + RT\ln\frac{c^M_{eq}}{\mathrm{C}} - RT\ln\frac{\mathrm{C}-c^M_{eq}}{\mathrm{C}},$$

$$\mu^M_{e,eq} = \frac{N_A^{5/3}\hbar^2(3\pi^2)^{2/3}}{2m_e}\left(c^M_{eq}\right)^{2/3},$$

$$B^O_v = B^O_e = \frac{RT\mathrm{C}}{c^O_{eq}\left(\mathrm{C}-c^O_{eq}\right)}, \tag{A1}$$

$$B^M_v = \frac{RT\mathrm{C}}{c^M_{eq}\left(\mathrm{C}-c^M_{eq}\right)}, \tag{A2}$$

$$B^M_e = \frac{2}{3}\frac{\mu^M_{e,eq}}{c^M_{eq}}. \tag{A3}$$

The difference in equilibrium chemical Gibbs free energy densities $\Delta G^\circ \equiv G^{\circ M} - G^{\circ O}$ is given by

$$\begin{aligned}\Delta G^\circ = {}& \mathrm{C}\left(\mu^{\circ M}_m - \mu^{\circ O}_m - \mu^{\circ O}_a\right) + \frac{3}{5}c^M_{eq}\mu^M_{e,eq} \\ & + \left(\mathrm{C}-c^M_{eq}\right)\left[\mu^{\circ M}_{\{a\}} + RT\left(\frac{c^M_{eq}}{\mathrm{C}-c^M_{eq}}\ln\frac{c^M_{eq}}{\mathrm{C}} + \ln\frac{\mathrm{C}-c^M_{eq}}{\mathrm{C}}\right)\right] \\ & - \sum_{i=v,e} c^O_{eq}\left[\mu^{\circ O}_{\{i\}} + RT\left(\ln\frac{c^O_{eq}}{\mathrm{C}} + \frac{\mathrm{C}-c^O_{eq}}{c^O_{eq}}\ln\frac{\mathrm{C}-c^O_{eq}}{\mathrm{C}}\right)\right].\end{aligned} \tag{A4}$$

APPENDIX B: DEBYE LENGTH AND SCREENING LENGTH

The Debye length in the oxide is derived by assuming constant defect electrochemical potentials in the oxide in the presence of a spatially varying electrostatic potential [27]. This allows us to solve for the functional form of the electrostatic potential in the oxide by solving the homogeneous solution to Gauss's law. We use a constant $\mathcal{C}$ to absorb terms independent of ψ. The electrostatic potentials in the system as defined

in Eq. (9), assuming constant electrochemical potentials at equilibrium, are given by

$$\begin{aligned}\bar{\mu}_i^O &= \frac{\delta G^O}{\delta c_i} + \psi q_i F \\ &= \mu_{i,eq}^O + B_i^O\left(c_i - c_{eq}^O\right) + \psi q_i F = \mathcal{C},\end{aligned}$$

which we can use to solve for the functional form of the equilibrium density profiles:

$$\Rightarrow c_i = -\frac{q_i F}{B_i^O}\psi + \mathcal{C}. \tag{B1}$$

The charge density in the system defined by Eq. (5) is $\rho = (c_v - c_e)F$. Substituting Eq. (B1) into ρ yields

$$\rho = -F^2\left(\frac{1}{B_v^O} + \frac{1}{B_e^O}\right)\psi + \mathcal{C}.$$

We can now find the homogeneous solution to Gauss's law:

$$\begin{aligned}\varepsilon^O\nabla^2\psi &= -\rho, \\ \nabla^2\psi &= -\frac{F^2}{\varepsilon^O}\left(\frac{1}{B_v^O} + \frac{1}{B_e^O}\right)\psi + \mathcal{C} \\ &\Rightarrow \psi \propto \exp\left(-\frac{x}{L_D}\right), \\ \text{where}\quad L_D &= \left[\frac{F^2}{\varepsilon^O}\left(\frac{1}{B_v^O} + \frac{1}{B_e^O}\right)\right]^{-1/2}.\end{aligned}$$

The Debye length L_D characterizes the decay length of space charge, electrostatic potential, and electric field in the oxide, and reflects the coupling of the electrostatics to the chemical free energy of the charged defects. If we substitute B_v^O and B_e^O from Eq. (A1) into the Debye length we have

$$L_D = \sqrt{\frac{RT\mathrm{C}\varepsilon^O}{2c_{eq}^O\left(\mathrm{C} - c_{eq}^O\right)F^2}},$$

which agrees exactly with the classical Debye length given in Eq. (1) in the dilute limit.

The screening length in the metal, L_S, can be derived in an analogous fashion, resulting in

$$\begin{aligned}\psi &\propto \exp\left(-\frac{x}{L_S}\right), \\ \text{where}\quad L_S &= \left[\frac{F^2}{\varepsilon^M}\left(\frac{1}{B_v^M} + \frac{1}{B_e^M}\right)\right]^{-1/2}.\end{aligned}$$

Substituting Eqs. (A2) and (A3) into the screening length yields

$$L_S = \left[\frac{F^2}{\varepsilon^M}\left(\frac{c_{eq}^M\left(\mathrm{C} - c_{eq}^M\right)}{RT\mathrm{C}} + \frac{3m_e\left(c_{eq}^M\right)^{\frac{1}{3}}}{N_A^{\frac{5}{3}}\hbar^2(3\pi^2)^{\frac{2}{3}}}\right)\right]^{-\frac{1}{2}}. \tag{B2}$$

Examining the metal's screening length L_S, as the density of anions in the metal becomes very small ($c_{eq}^M/\mathrm{C} \approx 1$), their contribution to the screening in the metal goes to zero. In this case, the screening length approaches the Thomas-Fermi screening length [35].

APPENDIX C: ELECTROSTATIC INTERFACIAL ENERGY

The electrostatic interfacial energy in the sharp interface description can be derived by calculating the total energy of the equilibrium defect density profiles, charge density, and electrostatic potential given by Eqs. (29), (32), and (35). As in Sec. IV, we consider the oxide-metal sharp interface to be at $x = 0$, with the oxide and metal extending to $x = -\infty$ and $x = \infty$, respectively, and the electrostatic potential in the bulk oxide to be 0. This treatment is therefore valid in the Wagner regime, where the charge density decays to zero on a length scale much smaller than the oxide thickness:

$$\begin{aligned}\gamma_\psi &= \int_{-\mathrm{inf}}^{0}\left[G^O\left(c_v^O, c_e^O\right) + \frac{1}{2}\rho^O\psi^O\right]dx \\ &\quad + \int_0^{\mathrm{inf}}\left[G^M\left(c_v^M, c_e^M\right) - \Delta G^\circ + \frac{1}{2}\rho^M\psi^M\right]dx \\ &= \frac{1}{2}\left(\frac{L_D}{\varepsilon^O} + \frac{L_S}{\varepsilon^M}\right)^{-1}\left[\frac{\left(B_e^M - B_v^M\right)\left(\mu_{e,eq}^M + \mu_{v,eq}^M\right)}{F\left(B_e^M + B_v^M\right)}\right. \\ &\quad \left. - \Delta\psi^\circ\right]\Delta\psi^\circ.\end{aligned} \tag{C1}$$

Substituting Eq. (34) into (C1) yields

$$\gamma_\psi = \frac{1}{2}\left[\frac{\left(B_e^M - B_v^M\right)\left(\mu_{e,eq}^M + \mu_{v,eq}^M\right)}{F\left(B_e^M + B_v^M\right)} - \Delta\psi^\circ\right]\sigma^O. \tag{C2}$$

APPENDIX D: FREE ENERGY PARTIAL DERIVATIVES

The nondimensionalized versions of the evolution equations (51) and (52) are given by

$$\begin{aligned}\frac{\partial\phi}{\partial t} &= M_\phi\left(2A\phi(-2\phi^2 + 3\phi - 1) + \epsilon\nabla^2\phi - \frac{\partial p(\phi)}{\partial\phi}\left\{\Delta G^\circ + \sum_{i=v,e}\left[-\mu_{i,eq}\left(c_{eq}^M - c_{eq}^O\right) + \frac{B_i^O B_i^M}{B_i}\left(\frac{\left(B_i^M - B_i^O\right)}{2B_i}(c_i - c_{eq})\right.\right.\right.\right. \\ &\quad \left.\left.\left.\left. - \frac{1}{B_i}q_i\mathrm{C}\Delta\psi^\circ - \left(c_{eq}^M - c_{eq}^O\right)\right)(c_i - c_{eq}) + \frac{\mathrm{C}^2}{2}(\Delta\psi^\circ)^2\frac{[1 - p(\phi)]^2 B_i^M - p(\phi)^2 B_i^O}{(B_i)^2}\right]\right\} - \frac{1}{2}\frac{\partial\varepsilon}{\partial\phi}|\nabla\psi|^2\right),\end{aligned} \tag{D1}$$

$$\frac{\partial c_v}{\partial t} = M_v\nabla^2\left[\mu_{v,eq} + \frac{B_v^O B_v^M}{B_v}(c_v - c_{eq}) + \mathrm{C}\psi\right], \tag{D2}$$

$$\frac{\partial c_e}{\partial t} = M_e\nabla^2\left[\mu_{e,eq} + \frac{B_e^O B_e^M}{B_e}(c_e - c_{eq}) - \mathrm{C}\psi\right]. \tag{D3}$$

[1] R. Mévrel, Mater. Sci. Eng. A **120-121**, 13 (1989).
[2] G. Meetham, J. Mater. Sci. **26**, 853 (1991).
[3] F. Pettit and G. Meier, in *Superalloys*, edited by M. Gell, C. Kartovich, R. Bricknel, W. Kent, and J. Radovich (The Metal Society AIME, Warrendale, PA, 1984), p. 651.
[4] A. Velon and I. Olefjord, Oxid. Met. **56**, 425 (2001).
[5] C. S. Giggins and F. S. Pettit, J. Electrochem. Soc. **118**, 1782 (1971).
[6] T. J. Nijdam, N. M. van der Pers, and W. G. Sloof, Mater. Corros. **57**, 269 (2006).
[7] P. Saltykov, O. Fabrichnaya, J. Golczewski, and F. Aldinger, J. Alloys Compd. **381**, 99 (2004).
[8] R. T. Wu, R. Zhu, L. T. Wu, Y. M. Nie, R. C. Reed, K. Kawagishi, and H. Harada, Can. Metall. Q. **50**, 291 (2011).
[9] B. E. Deal and A. S. Grove, J. Appl. Phys. **36**, 3770 (1965).
[10] C. Wagner, Corros. Sci. **13**, 23 (1973).
[11] A. Atkinson, Rev. Mod. Phys. **57**, 437 (1985).
[12] Z. Xu, K. M. Rosso, and S. Bruemmer, Phys. Chem. Chem. Phys. **14**, 14534 (2012).
[13] N. Cabrera and N. F. Mott, Rep. Prog. Phys. **12**, 163 (1949).
[14] C. Wagner, Z. Physik. Chem. (B) **21**, 25 (1933).
[15] V. Battaglia, J. Electrochem. Soc. **142**, 1423 (1995).
[16] N. Provatas and K. Elder, *Phase-Field Methods in Materials Science and Engineering*, 1st ed. (Wiley-VCH, Weinheim, Germany, 2010).
[17] S. G. Kim, W. T. Kim, and T. Suzuki, Phys. Rev. E **60**, 7186 (1999).
[18] I. Steinbach, F. Pezzolla, B. Nestler, M. Seeßelberg, R. Prieler, G. Schmitz, and J. Rezende, Phys. D (Amsterdam, Neth.) **94**, 135 (1996).
[19] R. Kobayashi, J. A. Warren, and W. C. Carter, Phys. D (Amsterdam, Neth.) **119**, 415 (1998).
[20] M. Asle Zaeem and H. El Kadiri, Comput. Mater. Sci. **89**, 122 (2014).
[21] A. T. Fromhold, Oxid. Met. **13**, 475 (1979).
[22] J. E. Guyer, W. J. Boettinger, J. A. Warren, and G. B. McFadden, Phys. Rev. E **69**, 021603 (2004).
[23] J. E. Guyer, W. J. Boettinger, J. A. Warren, and G. B. McFadden, Phys. Rev. E **69**, 021604 (2004).
[24] T.-l. Cheng, Y.-h. Wen, and A. Hawk, J. Phys. Chem. C **118**, 1269 (2014).
[25] L. Hong, J.-M. Hu, K. Gerdes, and L.-Q. Chen, J. Power Sources **287**, 396 (2015).
[26] K. R. Lawless, Rep. Prog. Phys. **37**, 231 (1974).
[27] K. Kliewer and J. Koehler, Phys. Rev. **140**, A1226 (1965).
[28] U. Aschauer, P. Bowen, and S. C. Parker, Acta Mater. **57**, 4765 (2009).
[29] J. Maier, J. Am. Ceram. Soc. **76**, 1212 (1993).
[30] M. H. R. Lankhorst, H. J. M. Bouwmeester, and H. Verweij, J. Am. Ceram. Soc. **80**, 2175 (1997).
[31] S. K. Mohapatra and F. A. Kröger, J. Am. Ceram. Soc. **61**, 106 (1978).
[32] A. Heuer, T. Nakagawa, M. Azar, D. Hovis, J. Smialek, B. Gleeson, N. Hine, H. Guhl, H.-S. Lee, P. Tangney, W. Foulkes, and M. Finnis, Acta Mater. **61**, 6670 (2013).
[33] F. Zhou, T. Maxisch, and G. Ceder, Phys. Rev. Lett. **97**, 155704 (2006).
[34] J. Honig, J. Chem. Educ. **43**, 76 (1966).
[35] J. J. Quinn and K.-S. Yi, in *Solid State Physics: Principles and Modern Applications* (Springer, Berlin, 2009), pp. 79–107.
[36] S. Mrowec and Z. Grzesik, J. Phys. Chem. Solids **65**, 1651 (2004).
[37] L. B. Loeb, in *Static Electrification* (Springer, Berlin, 1958), pp. 32–58.
[38] J. Maier, Solid State Ionics **23**, 59 (1987).
[39] T. Robert, M. Bartel, and G. Offergeld, Surf. Sci. **33**, 123 (1972).
[40] L. Mulay and L. Keys, J. Am. Chem. Soc. **87**, 1192 (1965).
[41] A. T. Dinsdale, CALPHAD **15**, 317 (1991).
[42] M. Z. Bazant, Acc. Chem. Res. **46**, 1144 (2013).
[43] E. Gongadze, S. Petersen, U. Beck, and U. V. Rienen, *COMSOL Conference 2009 (Milan)* (COMSOL, Milan, Italy, 2009).
[44] D. C. Grahame, Chem. Rev. **41**, 441 (1947).
[45] S. L. Wang, R. F. Sekerka, A. A. Wheeler, B. T. Murray, S. R. Coriell, R. J. Braun, and G. B. McFadden, Phys. D (Amsterdam, Neth.) **69**, 189 (1993).
[46] J. Eiken, B. Böttger, and I. Steinbach, Phys. Rev. E **73**, 066122 (2006).
[47] N. Moelans, Acta Mater. **59**, 1077 (2011).
[48] A. A. Wheeler, W. J. Boettinger, and G. B. McFadden, Phys. Rev. A **45**, 7424 (1992).
[49] M. Stengel and N. A. Spaldin, Nature (London) **443**, 679 (2006).
[50] J. Antula, Phys. Lett. **25**, 308 (1967).
[51] L. Y. Chen, *8th Int. Conf. Electron. Packag. Tech.* (IEEE, Shanghai, China, 2007).
[52] N. Ashcroft and N. Mermin, *Solid State Physics* (Saunders College, Philadelphia, PA, 1976).
[53] D. D. MacDonald, Electrochim. Acta **56**, 1761 (2011).